Nanostructured Block Copolymer Muscles

Chao Lang,[a,b,c] Elisabeth C. Lloyd,[b] Kelly E. Matuszewski,[b] Yifan Xu,[b] Venkat Ganesan,[d] Rui Huang,[e] Manish Kumar,[f] Robert J. Hickey[b,g,*]

[a]South China Advanced Institute for Soft Matter Science and Technology, School of Emergent Soft Matter, South China University of Technology, Guangzhou 510640, China.

[b]Materials Science and Engineering, The Pennsylvania State University, University Park, PA, USA

[c]Guangdong Provincial Key Laboratory of Functional and Intelligent Hybrid Materials and Devices, South China University of Technology, Guangzhou 510640, China.

[d]McKetta Department of Chemical Engineering, The University of Texas at Austin, Austin, TX 78712, USA

[e]Department of Aerospace Engineering and Engineering Mechanics, University of Texas at Austin, Austin, TX 78712, USA

[f]Department of Civil, Architectural and Environmental Engineering, University of Texas at Austin, Austin, TX 78712, USA

[g]Materials Research Institute, The Pennsylvania State University, University Park, PA, USA

*Corresponding author: rjh64@psu.edu

Abstract

High-performance actuating materials are necessary for advances in robotics, prosthetics, and smart clothing. Here, we report a class of fiber actuators by combining solution-phase block copolymer self-assembly and strain-programmed crystallization. The actuators consist of highly aligned nanoscale structures with alternating crystalline and amorphous domains, resembling the ordered and striated pattern of mammalian skeletal muscle. The reported nanostructured block copolymer muscles excel in several aspects as compared to current actuators, including efficiency (75.5%), actuation strain (80%), and mechanical properties (e.g., strain-at-break of up to 900% and toughness of up to 121.2 MJ/m^3). The fibers exhibit on/off rotary actuation with a peak rotational speed of 450 rpm. Furthermore, the reported

fibers demonstrate multi-trigger actuation (heat and hydration), offering switchable mechanical properties and various operating modes. The versatility and recyclability of the polymer fibers, combined with the facile fabrication method, opens new avenues for creating multifunctional and recyclable actuators using block copolymers.

Introduction

Biological tissues are intricately and hierarchically structured for specific functions and provide inspiration for creating novel materials exhibiting remarkable properties[1-4]. For example, natural structural materials such as silk[3], nacre[5], bone, and tooth[6] display unique mechanical properties due to the hierarchically ordered hard and soft phases[7]. Beyond static properties, living materials also exhibit energy-efficient and high-precision dynamic responses to the environment[8-10]. A notable example is mammalian skeletal muscles. With the ability to voluntarily generate force or produce movement, skeletal muscles are well-known for their multilevel hierarchical structures, especially the characteristic highly ordered and striated patterns at the single cell (muscle fiber) level[11] (**Fig. 1a**). Importantly, the actuation performance of muscles is directly related to their structural order, where disorder of the structure leads to drastic failure of function[12].

Inspired by natural muscles, artificial muscles and biomimetic actuators have the potential to revolutionize the fields of robotics[13, 14], prosthetic limbs[15], and smart clothing[16-18], leading to their rapid development in recent years[19-22]. While significant progress has been made in terms of replication of the actuating function of muscle fibers[20-24], mimicking the structure-function interplay has been largely ignored. An opportunity in the development of artificial muscles is correlating high-performance actuating materials with structural designs based on natural skeletal muscle fibers. In this respect, nanoscale block copolymer self-assembly is an ideal tool due to its broad structural palette and well-established guiding theories[25, 26]. As synthetic strategies and versatility of chain architectures advance, numerous applications are being developed for bulk and solution-phase nanoscale self-assembled block copolymers[27, 28], ranging from daily use in commodities such as adhesives, coatings, and packaging[28, 29], to highly engineered products such as therapeutic administration[30, 31], organic electronics[32, 33], and separation membranes[34-36].

Here, we report an innovative strategy for developing nanostructured actuating materials that bear surprising resemblance to both the structure and the function of mammalian skeletal muscle fibers. Reversible and recyclable polymer actuators are enabled by the use of nanostructured block copolymers. The combination of solution-phase block copolymer self-assembly and subsequent strain-programmed crystallization (SPC) was used to fabricate a new class of high-performance soft actuator/artificial muscle fibers. The exceptional actuation efficiency, actuation strain, and mechanical properties, which has yet to be reported, are

attributed to the highly aligned nanometer-scaled fiber microstructure, containing alternating crystalline and amorphous domains. Through implantation of both linear and rotational actuation movements with different stimuli-responses, as well as demonstration of continuous and switchable operating modes, we further highlight the versatility and potential of the reported actuating materials.

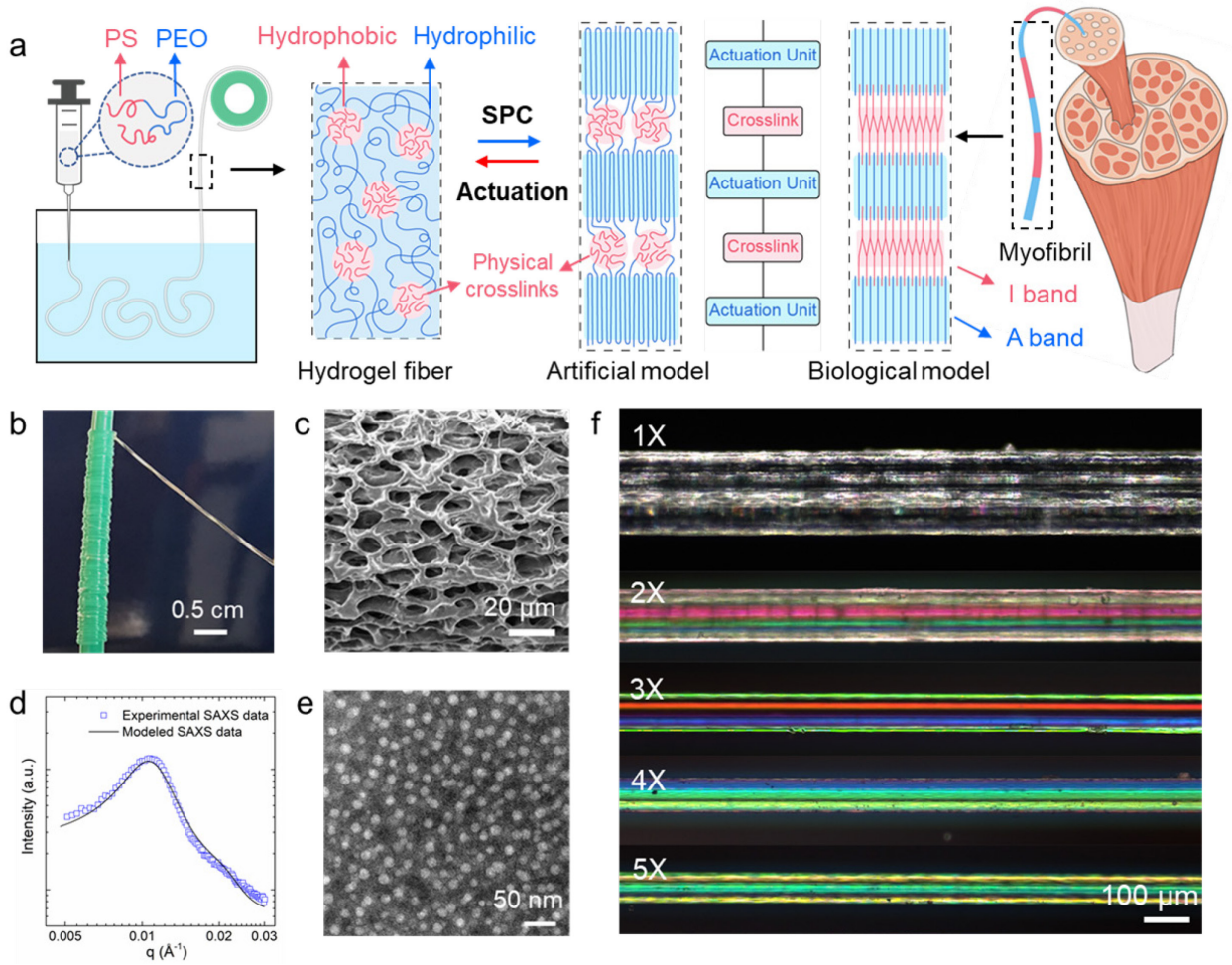

Fig. 1. Fiber fabrication through strain-programmed crystallization (SPC) of hydrogels created from self-assembled ABA triblock copolymers. (a) A scheme depicting the fiber preparation process and structural comparison between artificial model of SOS fibers and biological model of muscle myofibrils. (b) A one-meter-long hydrogel fiber made from rapid-injection processing using a SOS triblock copolymer. The ABA-type polymer chain architecture where the A-end blocks are glassy and the B-mid block is semi-crystalline is essential for creating mechanically robust hydrogel fibers[37, 38]. (c) SEM images of a freeze-dried hydrogel fiber, which exhibit interconnected cellular network structures at the micrometer scale. (d) SAXS data of the hydrogel fiber was modeled using a spherical form factor and a Percus–Yevick structure factor[39], which indicates a structure of disordered sphere at the nanometer scale. (e) TEM image of the SOS microgel shows disordered spheres resulting from the self-assembly procedure. (f) DIC images show that the 1X-5X fibers are uniform after crystallization under straining conditions and the alignment of the fibers increases along the fiber axis with increasing elongation ratios.

Fabrication of strained fibers

We adopted a facile two-step fabrication method to create biomimetic actuating fibers. The first step is to prepare uniform hydrogel fibers using the recently described rapid-injection method[39] where a 22 wt% THF solution of poly(styrene)-*b*-poly(ethylene oxide)-*b*-poly(styrene) (SOS) is injected into a water bath to trigger self-assembly (**Fig. 1a, 1b**). The linear ABA-type triblock copolymer SOS was synthesized by sequential living anionic polymerization followed by a coupling step, which afforded polymers with a number-average molecular weight (M_n) of 77 kg/mol, a PEO volume fraction of 75%, and a low molecular weight dispersity ($Đ$) of 1.07 (**Fig. S1, Table S1**). The narrow $Đ$ enables enhanced control over the self-assembly process[40], which is helpful for mimicking the long-range-ordered structure of muscle fibers[41]. Rapid-injection is an easy and versatile way for preparing physically crosslinked hydrogels with exceptional mechanical properties and hierarchical structures[39]. The rapid-injection hydrogel fibers are transparent and uniform in diameter (**Fig. S3, S5**). At the micrometer scale, SEM images of the freeze-dried hydrogel fibers indicate that the polymers form an interconnected cellular network, which forms as a result of the rapid-injection induced phase separation (**Fig. 1c**). At the nanometer scale, the as-prepared hydrogels display spherical micelle structures formed by aggregation of the hydrophobic poly(styrene) blocks, which were characterized using small-angle X-ray scattering (SAXS) (**Fig. 1d**). The scattering pattern was modeled with a spherical form factor and a Percus–Yevick structural factor (**Fig. 1d, Table S2**)[42]. The disordered structures of the crosslinked spherical micelles are also imaged using TEM on microgel samples produced from rapid-injection processing (**Fig. 1e, S2**).

The second step is to strain the elastic hydrogel fibers along the fiber axis at specific extensions and induce O-block crystallization during drying to trap the low-entropy, stretched polymer chain state. The restoring mechanical energy is released when the O-block crystals undergo a melting transition to non-crystalline states on application of specific stimuli. The low O-block melting temperature ($T_m \approx 65$ °C) and excellent water solubility allow for fabrication of actuating materials with mild stimuli. The exceptional mechanical properties and high elongation-at-break values of the hydrogel fibers provide a wide processing window for controlling the properties of the final products. Here, we study fibers with an elongation ratio from one (1X) to five (5X) (**Fig. 1f, S3**). As expected, the diameters of the further processed fibers reduce significantly as the elongation ratio increases. (**Fig. 1f, S3**). Both scanning electron microscope (SEM) and differential interference contrast (DIC) microscope images

indicate that the strained fibers are uniform (**Fig. 1f, S3**). The two-step fabrication process to create aligned fibers does not introduce any new chemical crosslinks or additional components into the original ABA triblock copolymer, allowing the self-assembled material to be easily recycled and reused by simply re-dissolving in a good solvent[43]. Additionally, the fabrication process does not require special instruments and is easily scalable using wet-spinning processing, which has been widely applied in industry[44].

Here, SOS was selected as a model block copolymer system to illustrate and exemplify our design principles. Glassy hydrophobic PS end blocks leads to the formation of nanometer-scaled spherical micelles when in water, and serve as strong physical crosslinks. The hydrophilic semi-crystalline PEO mid-block with a suitable $T_{m,PEO}$ ($T_{m,PEO} < T_{g,PS}$) melt to initiate contractile/rotational actuation, and the amorphous PEO domain will absorb water vapor and lead to expansion. Following the same designing principle, we anticipate that there are numerous different polymers that will satisfy these stated requirements, which will further expand the functionality and property range of available soft actuator materials.

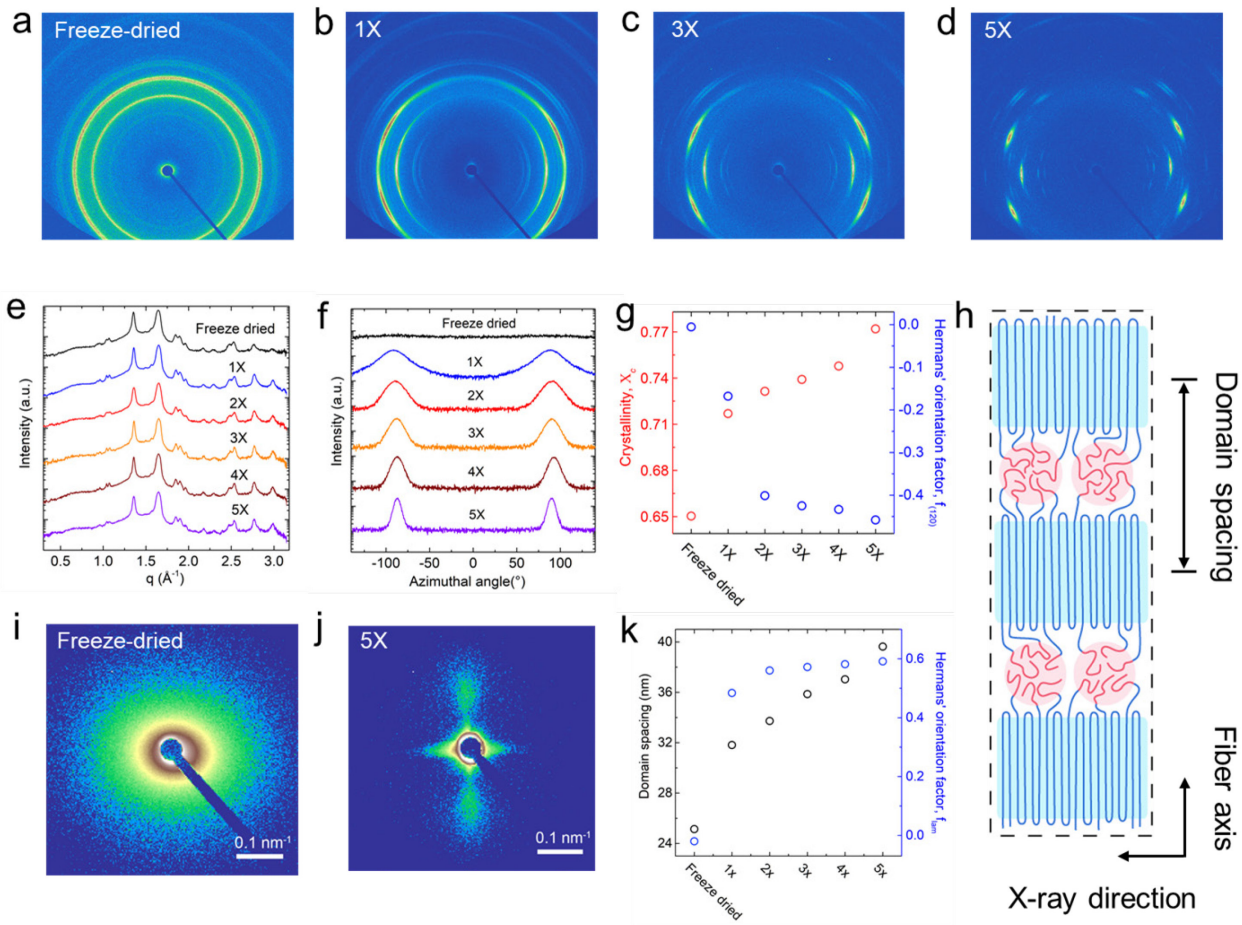

Fig. 2. SAXS and WAXS characterizations of strain processed fibers indicate that the structure is highly aligned and consists of alternating crystalline and amorphous domains. (a-d) 2D WAXS scattering results show that freeze-dried and 1X-5X fibers exhibit diffraction patterns characteristic of the O-block crystals. The crystal orientation in the fiber increases with increasing elongation ratio. (e) 1D WAXS scattering of fibers at different strains plotted together show the same crystal unit structure of O. (f) 1D scattering profiles from azimuthal angle integration of the 2D WAXS data indicate the crystal orientation at unit cell level in the fibers increases with increasing elongation ratio. (g) From freeze-dried to 5X fiber, the crystallinity increases and the Herman's orientation factor of the crystal plane (120), $f_{(120)}$, decreases from 0 to -0.46, suggesting that the (120) plane becomes increasingly parallel to the fiber direction. (h) A scheme showing the suggested fiber structure with alternating crystalline and amorphous domains. (i, j) 2D SAXS patterns of freeze-dried and 5X fibers indicate that the crystal orientation at the lamellar level increases with increasing elongation ratio. (k) Changes in domain spacing and the Herman's orientation factor of the lamellae, f_{lam}, of fibers with increasing extension ratio, indicating the orientation of the crystal lamellae becomes increasingly perpendicular to the fiber axis from freeze-dried to 5X.

Structure characterization of SOS fibers

The crystalline unit cell and lamellar orientation of the strained fibers was established using wide-angle and small-angle X-ray scattering (WAXS and SAXS, respectively). The existence of crystalline domains in the fibers were confirmed using differential scanning calorimetry (DSC, **Fig. S6**). On the first heating ramp, the 1X through 5X fibers show similar endothermic peaks around 65 °C, indicating the melting of O-block crystals. The crystallinity of the fibers increases with elongation ratios (**Fig. S6**), which are further confirmed with WAXS (**Fig. 2a-2g, S7**). The O-block crystallinity of the 5X fiber is 77%, which is 12% greater than that of the freeze-dried fiber (**Fig. 2g**). Two-dimensional WAXS patterns show no change in the O-block crystal structure throughout different samples (**Fig. 2a-2d, S7**), but demonstrate the orientation of the crystalline domains increase at the unit cell level with increasing elongation ratios. O-blocks in all the samples crystalized into monoclinic structure with $P2_1/a$ space group (**Fig. 2e**), which is consistent with previous studies[45, 46]. The orientation level of the PEO crystal in the fibers was quantified using Herman's orientation factor, which describes the relationship between the normal direction of a specific plane to a reference direction[47]. Using the fiber axis direction as the reference direction, the Herman's orientation factor of crystal plane (120), $f_{(120)}$ was calculated from the azimuthal intensity plot of the (120) reflection (**Fig. 2f**). $f_{(120)}$ increased from 0 for the freeze-dried fiber to -0.46 for the 5X fiber, indicating that the polymer chain alignment in the crystal structure increases with increasing elongation along the fiber axis (**Table S3**).

SAXS measurements were also performed on the fibers to study O-crystals at the lamellar level (**Fig. 2i, 2j, S8**). Variable temperature experiments indicate that the crystals melt between 60 °C and 70 °C (**Fig. S9, S10**), which is consistent with the DSC measurements. The lamellar orientation of the fibers exhibits the same trend as the orientation of the crystal unit cell, which increases with increasing elongation ratios (**Fig. 2i, 2j, S8**). By calculating the Herman's orientation factor of the lamellae, f_{lam}, we found the lamellar orientation changed from isotropic for freeze-dried fiber to perpendicular to fiber axis for 5X fiber (**Fig. 2k**), which is consistent with the evolving trend of $f_{(120)}$ from WAXS results. The one-dimensional SAXS scattering data also indicates the lamellar domain spacing increased significantly from 25.1 nm for freeze-dried to 39.6 nm for 5X fiber (**Fig. 2k**). Combined with the O-block volume fraction in the SOS polymer and O-block crystallinity values, the thickness of the amorphous region of 1X-5X fiber was calculated to vary between 15.6 and 17.8 nm. The domain size of the amorphous region corresponds well with the S-micelle core size of 16.1 nm observed with TEM (**Fig. 1e**).

The structural arrangement of glassy PS cores in the fiber was thus proposed in **Fig. 2h**, where the alternating O crystalline domains and glassy S cores are orientated along the fiber axis. The existence of the PS spheres was first demonstrated through SAXS characterization of the fibers after melting the O crystalline domains (**Fig. S11**). The fiber structure is further supported by SEM images of the post-stretched fibers, where different layers of S spheres were distinguishable in the fiber (**Fig. S4**). The fascinating structural arrangement of S spheres with O crystals is not only reminiscent of composite materials where nanoparticles were embedded in a semi-crystalline polymer matrix[48], but also simulate the striated appearance of skeletal muscle fibers. The striated pattern of muscle fiber is a result of lateral alignment of myofibrils, where highly ordered alternating dark (anisotropic, A) and light (isotropic, I) bands can be observed. The repeating unit between neighboring centers of I bands (Z disks) is defined as sarcomere, the length of which will change accordingly when the muscle fibers contract or being stretched[49, 50]. Similarly, in the strained SOS fibers, the crystalline domains melt under mild heating conditions, which will lead to the neighboring amorphous domains approaching each other and generating contraction forces (**Fig. 1a**).

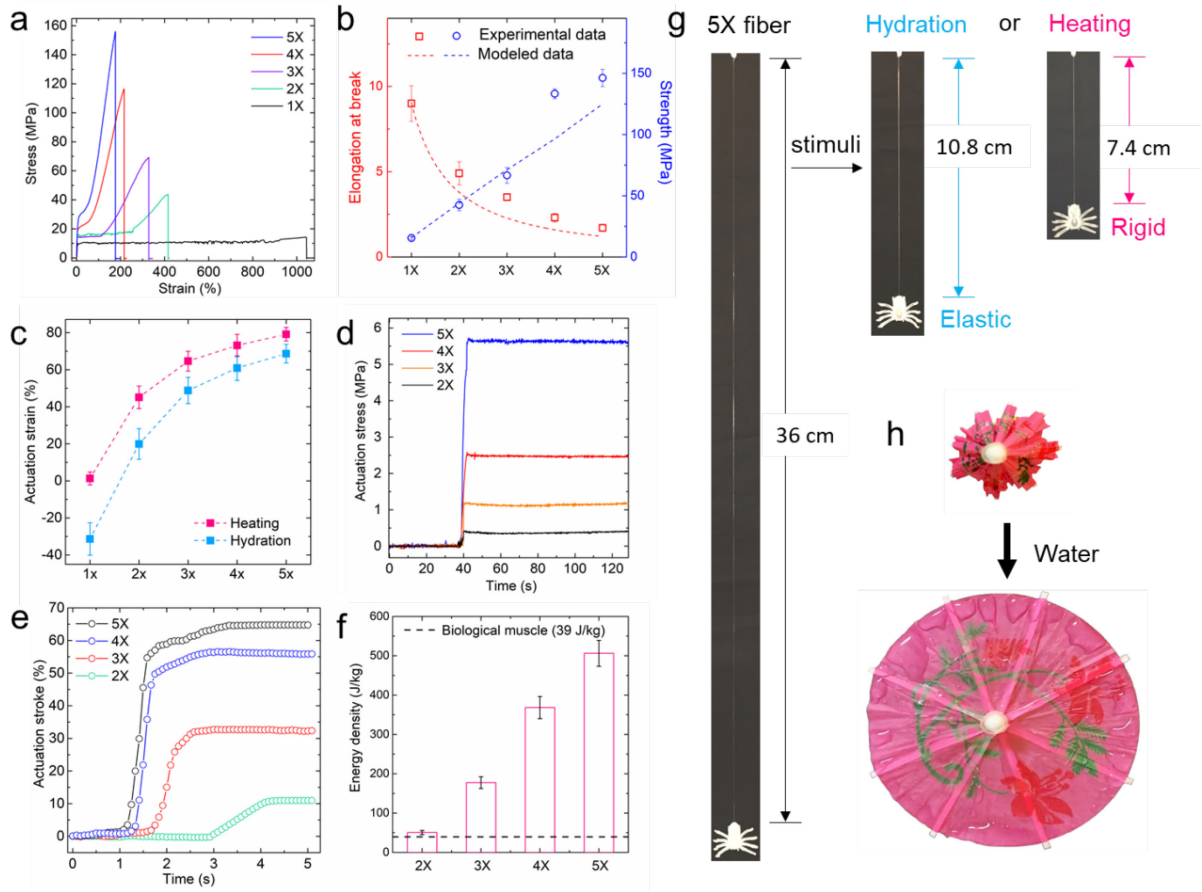

Fig. 3. Strained fibers exhibit exceptional mechanical and actuation properties. (a) Tensile test results of the fibers show decreased elongation at break values and increased tensile strength from 1X to 5X. The strain rate was 3/min. (b) Comparison of experimental and modeled mechanical properties of 1X to 5X fibers. (c) Length change of the fibers with different stimuli, where heating leads to contraction strain ranging from 0 to ~80%, and hydration leads to either expansion or contraction strain from about -30% to 70%. (d) The contractile actuation stress generated by 2X-5X fibers with hydration as the stimuli. (e) Actuation strain of fiber with hydration as stimuli while lifting up weight (0.31 g), which is more than 700 times of 5X fiber's own weight. (f) Energy density of 2X-5X fibers compared with mammalian skeletal muscle (39 J/kg). These values were calculated from fibers lifting up weight (0.31 g). (g) Photographs of 5X fibers before and after actuation. A small weight on the bottom of the fiber is used as a visual aid to help assess the fiber contraction. 5X fibers generate large actuation strain with both hydration and heating as stimuli, but display different mechanical properties after actuation. (h) An umbrella that autonomously opens when water is applied. 5X fibers were attached to the umbrella ribs for actuation.

Mechanical and actuation properties of SOS fibers

Uniaxial tensile measurements were conducted to establish the mechanical properties of the 1X-5X fibers (**Fig. 3a, S13**). The Young's modulus of the fibers increased significantly after the SPC procedure, ranging from 353 MPa to 608.2 MPa, which is over four orders of magnitude greater than that of the precursor hydrogel fiber (0.014 MPa, **Table S4)**. The elongation strain at break and strength of the fibers were found to vary with the strain programming elongation ratios. From 1X to 5X fiber, the elongation strain at break decreased from 900% to 170%, where the tensile strength increased from 15.5 to 146.2 MPa (**Table S4**). As a result, the 1X-5X fibers have similar toughness in the range from 103.2 to 121.2 MJ/m^3. These values are comparable to that of spider silk (70-160 MJ/m^3), which is characterized by their extraordinary toughness and biodegradability[3].

The mechanical properties of 1X-5X fibers were modeled using a composite microstructure consisting of three phases (e.g., crystalline PEO, amorphous PEO, and glassy PS (**Fig. S15a**)) and compared with experimental data (**Fig. 3b, S15, S16**). From 1X to 5X, the increase of crystallinity combined with decrease of porosity (**Fig. S14**) lead to decrease in fiber volume. Through the composite model, the Young's modulus values of the fibers are calculated considering the effects of crystallinity (**Fig. S15b**) and crystal orientation (**Fig. S16b**). The elongation at break and strength values were calculated based on the assumption that the true stress and total straining required to break the fibers are constants. The modeled data agreed well with the experimental data (**Fig. 3b, S16b**).

We then evaluated the actuation properties of 1X-5X fibers by first investigating the length change during contraction (without loading or attachment). We found that when heating is applied, the strained fibers contract to the expected theoretical value with actuation strains ranging from 0 to ~80% (**Fig. 3c, Fig. S20a**). In comparison, when hydration was used as stimuli, the strained fibers can display either expansion or contraction strain within the range from about -30% to 70% (**Fig. 3c**). This wide and tunable actuation range offers opportunities for various engineering applications, including the synthetic mimicry of natural muscle fibers, which contract 40% when isolated and 20% when attached (**Table S5**)[51]. Another noticeable feature is that the fibers display very different mechanical properties (**Table S4**) after actuation, which provides another dimension for engineering design. For example, contracted fibers are either solid and rigid after heating-triggered actuation due to the recrystallization of the O-domains when cooled back to room temperature, or soft and elastic similar to the starting

hydrogel fiber after hydration (**Fig. 3g**). The actuation stress generated by the fibers was then quantified using a load frame, which also shows an increasing trend from 1X to 5X (**Fig. 3d**). The 5X fibers can deliver an actuation stress of 5.5 MPa, which is 15 times greater than natural muscle fibers (**Table S5**)[51].

To quantify the work capacity of the strained fibers, weight-lifting tests were performed (**Fig. 3e, 3f, S18**). The actuation movement was quantified in detail through video analysis (**Fig. 3e, S18, Video S1, S2**). As expected, both the actuation strain and peak actuation speed of the fibers increase with increased elongation ratios (**Fig. 3e, S18**). Furthermore, the acceleration time was short, indicating that stored energy is rapidly released during actuation. Notably, the 5X fibers exhibit an actuation strain of 70% even when lifting an object greater than 700 times the fiber weight. Based on the same composite microstructure model for mechanical properties, the theoretical value of actuation strain triggered by heating was also calculated and exhibited the same trend as experimental values (**Fig. S20**). The energy density was then evaluated using the work done by the fibers and the fiber weight (**Fig. 3f**). All fibers exhibit high energy density, but the 5X fiber reaches a maximum of 506 J/kg in the series, which is more than ten times greater than mammalian skeletal muscle (39 J/kg, **Table S5**). Noticeably, these fibers perform actuation behaviors with high energy efficiency ranging from 40.5% to 75.5% with hydration as stimuli (**Fig. S19**), which is one of the highest among reported soft actuator/artificial muscle materials (**Table S5**). The radar figure in **Fig. S22** demonstrates a multi-dimensional comparison of material performance metrics for the reported fibers and previously published works on actuating artificial muscles. The reported nanostructured fibers outperform current actuating fibers on many levels, including tensile strain, toughness, actuation strain, and efficiency. To further demonstrate the versatility of the fibers, an umbrella that automatically opens when applying water was developed by simply attaching 5X fibers to the umbrella ribs. (**Fig. 3h, Video S3**).

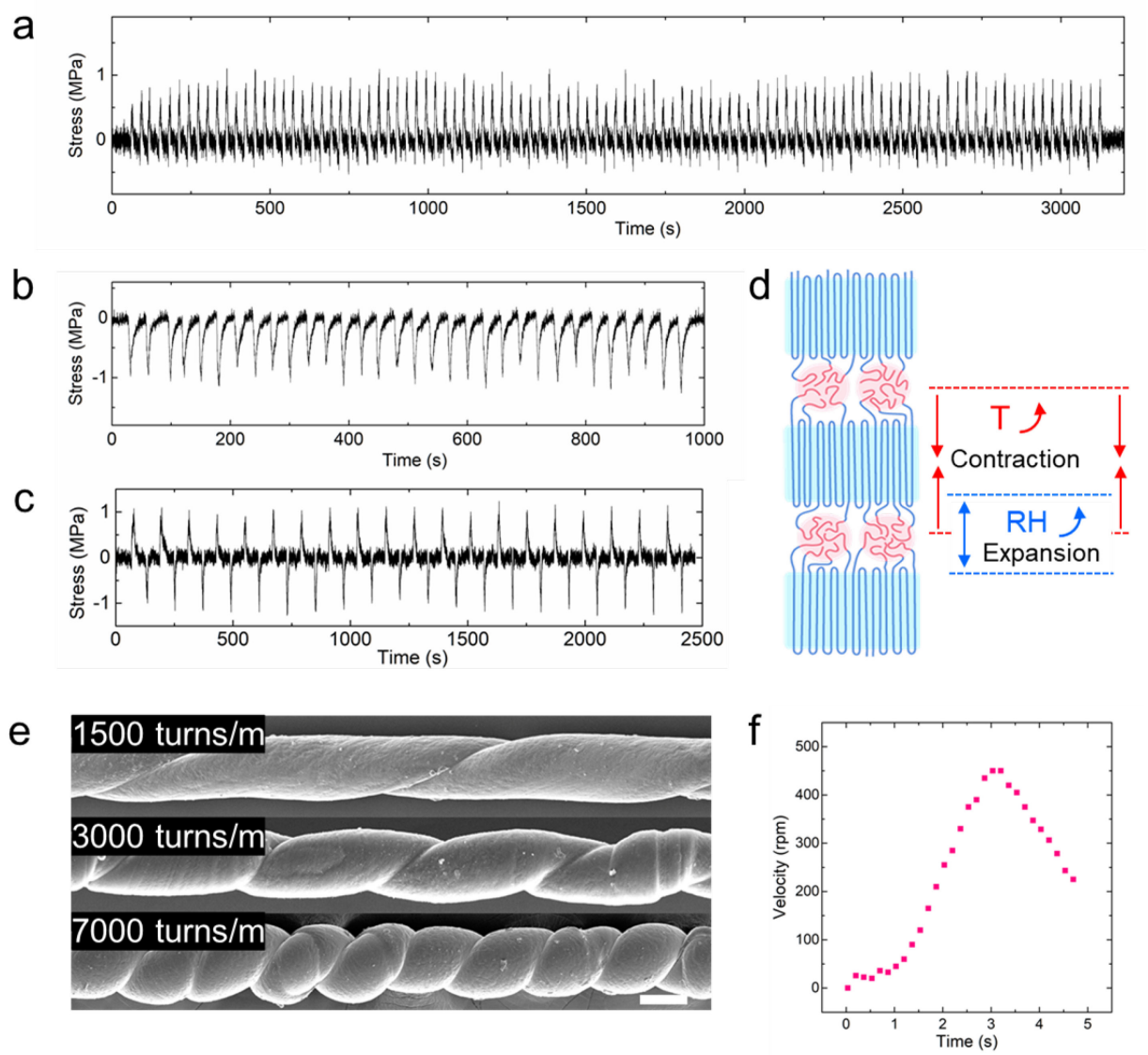

Fig. 4. Reversible and rotational actuation properties of strained fibers. (a) Reversible contractile actuation stress generation from 5X fiber at fixed length with heating as the stimuli. (b) Reversible expansional actuation stress generation from 5X fiber at fixed length by swelling and de-swelling of the amorphous domains with water vapor. (c) Alternating contractile and expansional actuation stress generation from 5X fiber at fixed length controlled by heating and water vapor. (d) A scheme displaying the mechanism of reversible actuation behaviors of the fibers triggered by heating and water vapor. (e) SEM of fibers with different twist degrees per length. Scale bar: 100 µm. (f) Rotational velocity from SOS fiber with a twist degree of 7000 turns/m where heating was used as stimuli.

Reversible and rotational actuation behaviors of SOS fibers

The reversible actuation behaviors of the fibers were then characterized by partially melting the crystalline domains via heating at fixed fiber length (i.e., constant strain). By controlling the heating temperature and time, 5X fibers were shown to generate a reversible contractile stress, where more than 100 actuation cycles were demonstrated without performance decline (**Fig. 4a**). The results indicate the potential of further applying these block copolymer fibers in real-world applications. Beyond contraction, we also found that the strained fibers can perform expansional actuation in a cyclic manner. When the relative humidity in the environment was varied (**Fig. S21**), the amorphous regions of the fibers can reversibly absorb and de-absorb water vapor, causing the fiber to generate reversible expansion stress (**Fig. 4b**). Here, water vapor is treated as a different stimulus from hydration, due to the opposite actuation responses of the SOS fibers and mechanism. Specifically, strained fibers exposed to water vapor over short time intervals (e.g., several seconds for our actuation experiment) lead to fiber expansion due to the water molecules swelling the amorphous PEO regions, but not melting the crystals. However, when the fiber sample is fully immersed in water (hydration), the PEO crystals melt, and the polymer fibers (2X-5X) contract due to the highly anisotropic nature of the structures. When both stimuli were used together, the fibers can generate either contraction or expansion stress as desired (**Fig. 4c**), making them more versatile actuators than natural muscle fibers (**Fig. 4d**). The dual-responsible feature is particularly appealing for building multimodal locomotive robots for completing tasks in complicated environments[14].

In addition to linear actuators made through straining, we also prepared rotational actuators by twisting the hydrogel fibers prior to crystallization. SEM images show that the rotational angles of the helical fibers are tuned by controlling the twist degree. (**Fig. 4e**). Similar to the linear actuators, rotational actuation is triggered via either hydration or heating (**Fig. 4f**), which was found to operate in continuous and switchable modes, respectively. Under hydration, the actuator works in a continuous fashion where constant rotational actuation will sustain until full energy release (**Video S4**). A peak rotational speed of 450 rpm was observed. Alternatively, heating offers better control, where actuation can be easily switched between on and off by applying or removing heating (**Video S5**). The rotational actuator is a demonstration of the versatility of this new type of actuating materials. In our previous study[39], we have shown that rapid-injection can be used for preparing hydrogels in different configurations such as coatings, printings, composites, and complex objects. We thus envision that the two-step fabrication

process is easily translated to many application scenarios where tough, high-performance, lightweight, and recyclable actuating materials are required.

Conclusions

Inspired by the structure and the function of muscle fibers, fiber actuators with highly aligned alternating amorphous and crystalline domains were prepared from ABA triblock copolymers. The glassy and semi-crystalline properties of the A and B blocks, respectively, which are necessary to mimic the structure and function of skeletal muscles, is easily translatable to different polymer compositions to satisfy materials requirements for specific applications. The fibers were fabricated using a two-step method, where hydrogel fibers made from rapid-injection processing were crystalized under strain to trap a low-entropy state. The fibers are recyclable due to a lack of chemical crosslinks, and yet display excellent mechanical properties, with toughness rivaling that of spider silk. The fibers also exhibit exceptional actuation behaviors, where the actuation strain, stress, energy density, and energy efficiency not only exceed the natural muscle fibers, but are also easily tuned. The reported nanostructured block copolymer fibers demonstrate both linear and rotational actuation movements that are triggered from three different stimuli (e.g., expansion in water vapor, and contraction/rotation in heating or hydration). Potential applications of such fibers include surgical robots, smart clothes, haptic and tactile interfaces, and prosthesis.

Acknowledgements

This work was supported by the Air Force Office of Scientific Research under the Young Investigator Prize (Award: 18RT0680, R.J.H.), National Science Foundation through the DMREF program (CMMI 2119717, R.J.H.), and the Materials Research Institute seed grant and start-up funds from the Penn State University (R.J.H.). M.K. was supported by National Science Foundation grant CBET 1946392 and the DMREF program CMMI 1627197. V. G. was supported in part by Welch Foundation (Grant F-1599). This research used the Complex Materials Scattering beamline of the National Synchrotron Light Source II, a U.S. Department of Energy (DOE) Office of Science User Facility operated for the DOE Office of Science by Brookhaven National Laboratory under Contract No. DE-SC0012704. TEM, SEM, SAXS, and WAXS measurements were taken at the Materials Characterization Lab (MCL) in the Materials Research Institute (MRI) at the Penn State University.

Author Contributions

C.L., M.K., and R.J.H. conceived the research. C.L. developed, prepared, and characterized materials. C.L. measured mechanical and actuation properties. E.C.L. and Y.X. conducted X-ray measurements. C.L. and K.E.M. analyzed actuation properties using video analysis. V.G.

and R.H. developed the mechanical property model. C.L., M.K., and R.J.H. wrote the manuscript. R.J.H. supervised the research. All authors read and commented on the manuscript.

Competing Interests

The authors declare no competing interests.

Figure Legends/Captions

Fig. 1. Fiber fabrication through strain-programmed crystallization (SPC) of hydrogels created from self-assembled ABA triblock copolymers. (a) A scheme depicting the fiber preparation process and structural comparison between artificial model of SOS fibers and biological model of muscle myofibrils. (b) A one-meter-long hydrogel fiber made from rapid-injection processing using a SOS triblock copolymer. The ABA-type polymer chain architecture where the A-end blocks are glassy and the B-mid block is semi-crystalline is essential for creating mechanically robust hydrogel fibers[37, 38]. (c) SEM images of a freeze-dried hydrogel fiber, which exhibit interconnected cellular network structures at the micrometer scale. (d) SAXS data of the hydrogel fiber was modeled using a spherical form factor and a Percus–Yevick structure factor[39], which indicates a structure of disordered sphere at the nanometer scale. (e) TEM image of the SOS microgel shows disordered spheres resulting from the self-assembly procedure. (f) DIC images show that the 1X-5X fibers are uniform after crystallization under straining conditions and the alignment of the fibers increases along the fiber axis with increasing elongation ratios.

Fig. 2. SAXS and WAXS characterizations of strain processed fibers indicate that the structure is highly aligned and consists of alternating crystalline and amorphous domains. (a-d) 2D WAXS scattering results show that freeze-dried and 1X-5X fibers exhibit diffraction patterns characteristic of the O-block crystals. The crystal orientation in the fiber increases with increasing elongation ratio. (e) 1D WAXS scattering of fibers at different strains plotted together show the same crystal unit structure of O. (f) 1D scattering profiles from azimuthal angle integration of the 2D WAXS data indicate the crystal orientation at the unit cell level in the fibers increases with increasing elongation ratio. (g) From freeze-dried to 5X fiber, the crystallinity increases and the Herman's orientation factor of the crystal plane (120), $f_{(120)}$, decreases from 0 to -0.46, suggesting that the (120) plane becomes increasingly parallel to the fiber direction. (h) A scheme showing the suggested fiber structure with alternating crystalline and amorphous domains. (i, j) 2D SAXS patterns of freeze-dried and 5X fibers indicate that

the crystal orientation at lamellar level increases with increasing elongation ratio. (k) Changes in domain spacing and the Herman's orientation factor of the lamellae, f_{lam}, of fibers with increasing extension ratio, indicating the orientation of the crystal lamellae becomes increasingly perpendicular to the fiber axis from freeze-dried to 5X.

Fig. 3. Strained fibers exhibit exceptional mechanical and actuation properties. (a) Tensile test results of the fibers show decreased elongation at break values and increased tensile strength from 1X to 5X. The strain rate was 3/min. (b) Comparison of experimental and modeled mechanical properties of 1X to 5X fibers. (c) Length change of the fibers with different stimuli, where heating leads to contraction strain ranging from 0 to ~80%, and hydration leads to either expansion or contraction strain from about -30% to 70%. (d) The contractile actuation stress generated by 2X-5X fibers with hydration as the stimuli. (e) Actuation strain of fiber with hydration as stimuli while lifting up weight (0.31 g), which is more than 700 times of 5X fiber's own weight. (f) Energy density of 2X-5X fibers compared with mammalian skeletal muscle (39 J/kg). These values were calculated from fibers lifting up weight (0.31 g). (g) Photographs of 5X fibers before and after actuation. A small weight on the bottom of the fiber is used as a visual aid to help assess the fiber contraction. 5X fibers generate large actuation strain with both hydration and heating as stimuli, but display different mechanical properties after actuation. (h) An umbrella that autonomously opens when water is applied. 5X fibers were attached to the umbrella ribs for actuation.

Fig. 4. Reversible and rotational actuation properties of strained fibers. (a) Reversible contractile actuation stress generation from 5X fiber at fixed length with heating as the stimuli. (b) Reversible expansional actuation stress generation from 5X fiber at fixed length by swelling and de-swelling of the amorphous domains with water vapor. (c) Alternating contractile and expansional actuation stress generation from 5X fiber at fixed length controlled by heating and water vapor. (d) A scheme displaying the mechanism of reversible actuation behaviors of the fibers triggered by heating and water vapor. (e) SEM of fibers with different twist degrees per length. Scale bar: 100 μm. (f) Rotational velocity from SOS fiber with a twist degree of 7000 turns/m where heating was used as stimuli.

Additional information

Correspondence and requests for materials should be addressed to R.J.H.

References

1. Vukusic P, Sambles JR. Photonic structures in biology. *Nature* 2003, **424**(6950)**:** 852-855.
2. Hamm CE, Merkel R, Springer O, Jurkojc P, Maier C, Prechtel K*, et al.* Architecture and material properties of diatom shells provide effective mechanical protection. *Nature* 2003, **421**(6925)**:** 841-843.
3. Omenetto FG, Kaplan DL. New Opportunities for an Ancient Material. *Science* 2010, **329**(5991)**:** 528-531.
4. Wong T-S, Kang SH, Tang SKY, Smythe EJ, Hatton BD, Grinthal A*, et al.* Bioinspired self-repairing slippery surfaces with pressure-stable omniphobicity. *Nature* 2011, **477**(7365)**:** 443-447.
5. Tang Z, Kotov NA, Magonov S, Ozturk B. Nanostructured artificial nacre. *Nat Mater* 2003, **2**(6)**:** 413-418.
6. Hannig M, Hannig C. Nanomaterials in preventive dentistry. *Nat Nanotechnol* 2010, **5**(8)**:** 565-569.
7. Wegst UGK, Bai H, Saiz E, Tomsia AP, Ritchie RO. Bioinspired structural materials. *Nat Mater* 2015, **14**(1)**:** 23-36.
8. Bell FI, McEwen IJ, Viney C. Supercontraction stress in wet spider dragline. *Nature* 2002, **416**(6876)**:** 37-37.
9. Capadona JR, Shanmuganathan K, Tyler DJ, Rowan SJ, Weder C. Stimuli-Responsive Polymer Nanocomposites Inspired by the Sea Cucumber Dermis. *Science* 2008, **319**(5868)**:** 1370-1374.
10. He X, Aizenberg M, Kuksenok O, Zarzar LD, Shastri A, Balazs AC*, et al.* Synthetic homeostatic materials with chemo-mechano-chemical self-regulation. *Nature* 2012, **487**(7406)**:** 214-218.
11. Lieber RL. *Skeletal muscle structure, function, and plasticity*, 2nd Ed edn. Lippincott Williams & Wilkins, 2002.
12. Puthucheary Z, Montgomery H, Moxham J, Harridge S, Hart N. Structure to function: muscle failure in critically ill patients. *The Journal of Physiology* 2010, **588**(23)**:** 4641-4648.
13. Li C, Lau GC, Yuan H, Aggarwal A, Dominguez VL, Liu S*, et al.* Fast and programmable locomotion of hydrogel-metal hybrids under light and magnetic fields. *Science Robotics* 2020, **5**(49)**:** eabb9822.
14. Hu W, Lum GZ, Mastrangeli M, Sitti M. Small-scale soft-bodied robot with multimodal locomotion. *Nature* 2018, **554**(7690)**:** 81-85.
15. Biddiss E, Chau T. Dielectric elastomers as actuators for upper limb prosthetics: Challenges and opportunities. *Medical Engineering & Physics* 2008, **30**(4)**:** 403-418.
16. Wang W, Yao L, Cheng C-Y, Zhang T, Atsumi H, Wang L*, et al.* Harnessing the hygroscopic and biofluorescent behaviors of genetically tractable microbial cells to design biohybrid wearables. *Science Advances* 2017, **3**(5)**:** e1601984.
17. Eschen K, Granberry R, Abel J. Guidelines on the design, characterization, and operation of shape memory alloy knitted actuators. *Smart Materials and Structures* 2020, **29**(3)**:** 035036.
18. Zhao H, Qi X, Ma Y, Sun X, Liu X, Zhang X*, et al.* Wearable Sunlight-Triggered Bimorph Textile Actuators. *Nano Lett* 2021, **21**(19)**:** 8126-8134.
19. Mirvakili SM, Hunter IW. Artificial Muscles: Mechanisms, Applications, and Challenges. *Adv Mater* 2018, **30**(6)**:** 1704407.
20. Kanik M, Orguc S, Varnavides G, Kim J, Benavides T, Gonzalez D*, et al.* Strain-programmable fiber-based artificial muscle. *Science* 2019, **365**(6449)**:** 145-150.
21. Mu J, Jung de Andrade M, Fang S, Wang X, Gao E, Li N*, et al.* Sheath-run artificial muscles. *Science* 2019, **365**(6449)**:** 150-155.
22. Yuan J, Neri W, Zakri C, Merzeau P, Kratz K, Lendlein A*, et al.* Shape memory nanocomposite fibers for untethered high-energy microengines. *Science* 2019, **365**(6449)**:** 155-158.
23. Chen P, Xu Y, He S, Sun X, Pan S, Deng J*, et al.* Hierarchically arranged helical fibre actuators driven by solvents and vapours. *Nat Nanotechnol* 2015, **10**(12)**:** 1077-1083.
24. Liu D, Tarakanova A, Hsu CC, Yu M, Zheng S, Yu L*, et al.* Spider dragline silk as torsional actuator driven by humidity. *Science Advances* 2019, **5**(3)**:** eaau9183.

25. Bates FS, Fredrickson G. Block copolymers-designer soft materials. *Phys Today* 1999, **52**(2)**:** 32-38.
26. Bates FS, Hillmyer MA, Lodge TP, Bates CM, Delaney KT, Fredrickson GH. Multiblock Polymers: Panacea or Pandora's Box? *Science* 2012, **336**(6080)**:** 434-440.
27. Mai Y, Eisenberg A. Self-assembly of block copolymers. *Chem Soc Rev* 2012, **41**(18)**:** 5969-5985.
28. Bates CM, Bates FS. 50th Anniversary Perspective: Block Polymers—Pure Potential. *Macromolecules* 2017, **50**(1)**:** 3-22.
29. Shin J, Martello MT, Shrestha M, Wissinger JE, Tolman WB, Hillmyer MA. Pressure-Sensitive Adhesives from Renewable Triblock Copolymers. *Macromolecules* 2011, **44**(1)**:** 87-94.
30. Jeong B, Bae YH, Lee DS, Kim SW. Biodegradable block copolymers as injectable drug-delivery systems. *Nature* 1997, **388**(6645)**:** 860-862.
31. Geng Y, Dalhaimer P, Cai S, Tsai R, Tewari M, Minko T*, et al.* Shape effects of filaments versus spherical particles in flow and drug delivery. *Nat Nanotechnol* 2007, **2**(4)**:** 249-255.
32. Bouchet R, Maria S, Meziane R, Aboulaich A, Lienafa L, Bonnet J-P*, et al.* Single-ion BAB triblock copolymers as highly efficient electrolytes for lithium-metal batteries. *Nat Mater* 2013, **12**(5)**:** 452-457.
33. Cho JH, Lee J, Xia Y, Kim B, He Y, Renn MJ*, et al.* Printable ion-gel gate dielectrics for low-voltage polymer thin-film transistors on plastic. *Nat Mater* 2008, **7**(11)**:** 900-906.
34. Tu Y-M, Song W, Ren T, Shen Y-x, Chowdhury R, Rajapaksha P*, et al.* Rapid fabrication of precise high-throughput filters from membrane protein nanosheets. *Nat Mater* 2020, **19**(3)**:** 347-354.
35. Phillip WA, Dorin RM, Werner J, Hoek EMV, Wiesner U, Elimelech M. Tuning Structure and Properties of Graded Triblock Terpolymer-Based Mesoporous and Hybrid Films. *Nano Lett* 2011, **11**(7)**:** 2892-2900.
36. Peinemann K-V, Abetz V, Simon PFW. Asymmetric superstructure formed in a block copolymer via phase separation. *Nat Mater* 2007, **6**(12)**:** 992-996.
37. Lang C, Ye D, Song W, Yao C, Tu Y-m, Capparelli C*, et al.* Biomimetic Separation of Transport and Matrix Functions in Lamellar Block Copolymer Channel-Based Membranes. *ACS Nano* 2019, **13**(7)**:** 8292-8302.
38. Lang C, Kumar M, Hickey RJ. Influence of block sequence on the colloidal self-assembly of poly(norbornene)-block-poly(ethylene oxide) amphiphilic block polymers using rapid injection processing. *Polym Chem* 2020, **11**(2)**:** 375-384.
39. Lang C, LaNasa JA, Utomo N, Xu Y, Nelson MJ, Song W*, et al.* Solvent-non-solvent rapid-injection for preparing nanostructured materials from micelles to hydrogels. *Nat Commun* 2019**:** 10:3855.
40. Lynd NA, Meuler AJ, Hillmyer MA. Polydispersity and block copolymer self-assembly. *Progress in Polymer Science* 2008, **33**(9)**:** 875-893.
41. Li M-H, Keller P, Yang J, Albouy P-A. An Artificial Muscle with Lamellar Structure Based on a Nematic Triblock Copolymer. *Adv Mater* 2004, **16**(21)**:** 1922-1925.
42. Taribagil RR, Hillmyer MA, Lodge TP. Hydrogels from ABA and ABC Triblock Polymers. *Macromolecules* 2010, **43**(12)**:** 5396-5404.
43. Garcia JM, Robertson ML. The future of plastics recycling. *Science* 2017, **358**(6365)**:** 870-872.
44. Kou L, Huang T, Zheng B, Han Y, Zhao X, Gopalsamy K*, et al.* Coaxial wet-spun yarn supercapacitors for high-energy density and safe wearable electronics. *Nat Commun* 2014, **5**(1)**:** 3754.
45. Zhu L, Cheng SZD, Calhoun BH, Ge Q, Quirk RP, Thomas EL*, et al.* Crystallization Temperature-Dependent Crystal Orientations within Nanoscale Confined Lamellae of a Self-Assembled Crystalline−Amorphous Diblock Copolymer. *J Am Chem Soc* 2000, **122**(25)**:** 5957-5967.
46. Takahashi Y, Tadokoro H. Structural Studies of Polyethers, (-(CH2)m-O-)n. X. Crystal Structure of Poly(ethylene oxide). *Macromolecules* 1973, **6**(5)**:** 672-675.

47. Ponçot M, Martin J, Chaudemanche S, Ferry O, Schenk T, Tinnes JP*, et al.* Complementarities of high energy WAXS and Raman spectroscopy measurements to study the crystalline phase orientation in polypropylene blends during tensile test. *Polymer* 2015, **80:** 27-37.
48. Zhao D, Gimenez-Pinto V, Jimenez AM, Zhao L, Jestin J, Kumar SK*, et al.* Tunable Multiscale Nanoparticle Ordering by Polymer Crystallization. *ACS Central Science* 2017, **3**(7)**:** 751-758.
49. Rall JA. What makes skeletal muscle striated? Discoveries in the endosarcomeric and exosarcomeric cytoskeleton. *Advances in Physiology Education* 2018, **42**(4)**:** 672-684.
50. Schneidereit D, Nübler S, Prölß G, Reischl B, Schürmann S, Müller OJ*, et al.* Optical prediction of single muscle fiber force production using a combined biomechatronics and second harmonic generation imaging approach. *Light: Science & Applications* 2018, **7**(1)**:** 79.
51. Madden JDW, Vandesteeg NA, Anquetil PA, Madden PGA, Takshi A, Pytel RZ*, et al.* Artificial muscle technology: physical principles and naval prospects. *IEEE Journal of Oceanic Engineering* 2004, **29**(3)**:** 706-728.

Methods

Synthesis and characterization of polystyrene-PEO-polystyrene (SOS)

The triblock copolymers (SOS) used in this study were synthesized by sequential living anionic polymerization followed by coupling the hydroxyl groups at the PEO end with α,α'-dibromo-p-xylene[1]. The synthesized polymers were characterized using nuclear magnetic resonance (NMR, Avance AV3HD 500 NMR spectrometer, Bruker) and size-exclusion chromatography (SEC, EcoSEC HLC-8320GPC, Tosoh Bioscience) with THF as the mobile phase. The SEC was equipped with a Wyatt DAWN Heleos-II eight-angle static light scattering (SLS) detector (Wyatt Technology).

Procedure for fiber preparation

The fibers were prepared by using a two-step fabrication process. The first step is to make hydrogel fibers using rapid-injection processing[1], which is a solution-phase self-assembly method for amphiphilic block polymers. The second step is a subsequent strain-programmed crystallization of the hydrogel fibers. The details of a typical fiber fabrication procedure are described as follows. A 22 wt% THF solution of SOS was first injected into an excess amount of water through a nozzle with an inner diameter of 0.51 mm at an injection rate of 5 mL min^{-1}, leading to the formation of hydrogel fibers. The hydrogel fibers were then strained at different elongation ratios, λ, ranging from 1 to 5 ($\lambda = L_S/L_0$, where L_0 and L_S are the initial and final

length of the hydrogel fibers respectively; the strain rate was 3 min^{-1}). The fibers were then allowed to dehydrate and crystalize at ambient conditions under constant strain with both ends marked and fixed, leading to 1X-5X samples with different degrees of strain programmed into the fiber. The freeze-dried fibers were prepared by quenching the hydrated hydrogel fibers into liquid nitrogen and freeze dried under high vacuum to preserve the hydrogel network backbone structure. The helical fibers were fabricated by fixing one end of the fiber and rotating the other end until desired twist degree was reached. Both ends of the fiber were then fixed and the fiber was allowed to dehydrate and crystallize at ambient conditions.

Differential scanning calorimetry (DSC)

The thermal properties of the fibers were characterized using a Thermal Analysis Q2000 DSC. To prepare the samples, approximately 5 mg of fibers were loaded into hermetic aluminum pans. Data from the first heating ramp under nitrogen atmosphere was collected. The samples were first equilibrated at 25 °C and then heated to 100 °C at a heating rate of 10 °C/min. The crystallinity of the sample was calculated using the following equation:

$$X_{c,\ SOS} = \frac{H_m}{H_m^{\infty}} \tag{1}$$

where H_m is measured heat of fusion and H_m^{∞} is the heat of fusion for an infinite PEO crystal (203 J/g). The crystallinity of the PEO can be further calculated using the following equation:

$$X_{c,\ PEO} = \frac{H_m}{H_m^{\infty}} \times \frac{1}{w_{PEO}} \tag{2}$$

where w_{PEO} is the weight fraction of PEO in block copolymer SOS.

X-ray scattering

Transmission SAXS and WAXS measurements of the freeze-dried and 1X-5X fiber samples were performed using a Cu Kα sourced (1.54 Å and 8.04 keV) Xeuss 2.0 (XENOCS) instrument installed with collimation optics and a 2D X-ray detector Pilatus3R 200K-A (Dectris). The scattering wavevector, q, was calibrated by using a standard sample of powder silver behenate. The fibers were placed vertically and measured under vacuum.

Synchrotron measurements were conducted at National Synchrotron Light Source II (NSLS-II) at Brookhaven National Laboratory using the Complex Materials Scattering (CMS/11-BM) beamline. Using a 13.50 keV beam (where the wavelength was 0.9184 Å), the hydrogel samples were exposed for 10 s at ambient conditions and artificial muscle fibers were exposed for 3 s under vacuum. The scattering images were captured with a Dectris Pilatus 2M detector, the sample to detector distance was 5 m.

Crystal orientation

The orientation levels of the PEO crystal in different fiber samples were quantified by orientation factor $<\cos^2\varphi>$ and Herman's orientation factor *f* using the following equations:

$$< \cos^2\varphi >= \frac{\int_0^{\frac{\pi}{2}} I(\varphi) \cos^2\varphi \sin\varphi \, d\varphi}{\int_0^{\frac{\pi}{2}} I(\varphi) \sin\varphi \, d\varphi} \quad (3)$$

$$f = \frac{3(\cos^2\varphi) - 1}{2} \quad (4)$$

where I(φ) is the scattering intensity by the (*hkl*) plane as a function of the azimuthal angle φ (relative to the reference direction). Significant values of $<\cos^2\varphi>$ and *f* are included in **Table S3**.

Modelling of the SAXS data

The SAXS data of hydrogel fibers and artificial muscle fibers were modeled using previously reported method[1-3]. For 1X and 2X, the samples were heated above the melting temperature of PEO with the fibers' both ends fixed, to only characterize the structure of the PS spheres. For the hydrogel samples, due to the low scattering length density difference between polystyrene (ρ_{PS} is 9.516×10^{10} cm^{-2}) and water (ρ_{water} = 9.441×10^{10} cm^{-2}), the scattering pattern of the hydrogel fiber was mainly attributed to the difference between the high PEO concentration in the micelle corona and the low PEO concentration in the hydrogel matrix. Similar to previous work[1-3], the scattering intensity profile can be simulated as the product of hard sphere form *P(q)* and disordered spherical structure factor, *S(q)*. The fitting parameters used in the model were

listed in **Table S2**.

Tensile test

Uniaxial tensile stress-strain tests were performed on an Instron 5866 load frame with a 10 N load cell. The samples were stretched at a constant strain rate of 3/min until fracture, and measurements were conducted in triplicate for each sample. Mechanical properties of the fibers were summarized in Table S4. The data obtained from the instrument were background-subtracted. The Young's modulus of the 1X-5X samples can be evaluated by fitting the initial part of the stress-strain curves using the following equation,

$$\sigma_{\text{eng}} = E\varepsilon_{eng} \tag{5}$$

where σ_{eng} is engineering stress, ε_{eng} is engineering strain, and E is Young's modulus. The Young's modulus of the hydrogel sample can be evaluated by fitting the initial part of the stress-strain curves using the following equation,

$$\sigma_{\text{eng}} = \frac{E}{3}\left(\lambda - \frac{1}{\lambda^2}\right) \tag{6}$$

where σ_{eng} is engineering stress, $\lambda = 1 + \varepsilon_{eng}$ is elongation ratio, and E is Young's modulus. In addition, the maximum engineering stress was taken as the strength, and the toughness was calculated by integrating the stress-strain curves.

Measurement of fiber actuation stress

To measure the stress generated by the fibers during actuation, both ends of a two-centimeter-long fiber were fixed to sample holders of the load frame, where one of the holders was attached to a fixed surface and the other one attached to the force transducer. While maintaining the distance between the two holders constant, water was applied to the fiber through spraying. The force reading from the transducer was then reordered, which can be further converted to stress using the initial cross-section area of the fibers. Measurements were conducted in triplicate for each sample (**Fig. S17**).

Fiber actuation movement quantification

The linear actuation movements of the fibers were quantified using the video analysis and modelling tool, Tracker 5.1.x (The Open Source Physics Project). The hanging weight was marked for movement tracking. The length scale of the video footage was first calibrated, and the marker position was set as the coordinate origin before the video was analyzed frame by frame. The rotational movement was quantified by analyzing the video with MATLAB code provided by MathWorks with minor modification. The rotational velocity was obtained by tracking the HSV color value changing times per frame, which can be then converted to rotations per minute using the frame rate of the video. The energy density was then calculated by using the work done by the fiber divided by the fiber mass. The energy efficiency of the fibers was estimated using the work performed by the fiber divided by the mechanical energy input during fiber straining, which can be characterized using tensile test (**Fig. S13**). Heating was applied using ceramic ionic flat irons (HSI Professional Glider), while water vapor was applied through polyurethane sponge strips. Hydration was applied by either submerging the sample into water with a glass cylinder (for contraction), or adding water to the sample with a syringe (for rotation).

Data availability

The datasets that support the finding of this study are available in ScholarSphere repository with the identifier(s) (https://doi.org/10.26207/tvbb-rf14). Source data are provided with this paper.

References

1. Lang C, LaNasa JA, Utomo N, Xu Y, Nelson MJ, Song W*, et al.* Solvent-non-solvent rapid-injection for preparing nanostructured materials from micelles to hydrogels. *Nat Commun* 2019**:** 10:3855.
2. Taribagil RR, Hillmyer MA, Lodge TP. Hydrogels from ABA and ABC Triblock Polymers. *Macromolecules* 2010, **43**(12)**:** 5396-5404.
3. Guo C, Bailey TS. Highly distensible nanostructured elastic hydrogels from AB diblock and ABA triblock copolymer melt blends. *Soft Matter* 2010, **6**(19)**:** 4807-4818.